Structures of [001] twist boundaries in gold. II. Results obtained by x-ray diffraction and computer simulation

I. Majid, P. D. Bristowe, and R. W. Balluffi
Department of Materials Science and Engineering, Massachusetts Institute of Technology, Cambridge, Massachusetts 02139
(Received 21 November 1988; revised manuscript received 27 February 1989)

Absolute grain-boundary structure factors, $|F_b|$, were measured for a series of [001] twist boundaries in gold by the x-ray-diffraction method described in the preceding paper. The series included the $\Sigma 113(\theta=7.6°)$, $\Sigma 25(\theta=16.3°)$, $\Sigma 13(\theta=22.6°)$, $\Sigma 17(\theta=28.1°)$, and $\Sigma 5(\theta=36.9°)$ boundaries (θ being the twist angle). The atomistic structures and $|F_b|$'s of these boundaries were also calculated by computer simulation using the embedded-atom model. The calculated atomic relaxations in the boundary cores consisted mainly of rotations around the O lattice elements, in agreement with previous work, and became monotonically weaker as θ increased. A considerable degree of consistency between measured and calculated $|F_b|$'s was obtained for all five boundaries. The calculated results faithfully tracked large measured decreases in $|F_b|$ as θ increased. Considerable consistency was found between measured and calculated sets of $|F_b|$'s for individual boundaries, particularly for $\Sigma 113$ and $\Sigma 25$, where the scattering was relatively strong. For the weakly scattering $\Sigma 5$ boundary, the observed $|F_b|$'s led to a most probable structure with small displacements which closely resembled the calculated structure. For the intermediate $\Sigma 13$ and $\Sigma 17$ boundaries, the limited number of measured $|F_b|$'s was reasonably consistent with calculated values. It was therefore concluded that the atomistic boundary structures calculated by the embedded-atom model were essentially correct. The present boundary structures were in quite good agreement with those of Fitzsimmons and Sass for $\Sigma 13$, but in strong disagreement for $\Sigma 5$, where their model possessed displacements that were much too large.

I. INTRODUCTION

In the preceding paper,[1] we described a method for experimentally determining absolute grain-boundary structure factors by means of x-ray diffractometry. The basis of the technique was outlined and the experimental procedures for carrying out the necessary measurements were described. In the present work, we apply the method to determine experimentally absolute structure factors for the series of [001] twist boundaries in gold, which includes the $\Sigma 113(\theta=7.6°)$, $\Sigma 25(\theta=16.3°)$, $\Sigma 13(\theta=22.6°)$, $\Sigma 17(\theta=28.1)$, and $\Sigma 5(\theta=36.9°)$ boundaries (θ is the twist angle). The atomistic structures (and structure factors) of these boundaries are also calculated by computer simulation using the embedded-atom model,[2] and the measured and calculated results are then compared in order to check for consistency. In addition, the results for the $\Sigma 13$ and $\Sigma 5$ boundaries are compared with previous measurements of relative structure factors and models for these boundaries obtained by Fitzsimmons and Sass.[3,4]

II. PREVIOUS STUDIES OF [001] TWIST BOUNDARY STRUCTURES

The structures of [001] twist boundaries in gold have been studied previously to various degrees by means of both transmission-electron microscopy[5,6] (TEM) and x-ray diffraction.[3,4,7–9] Direct TEM imaging[5,6] has shown that "low-angle" twist boundaries ($\theta \leq 20°$) consist of square grids of discrete localized lattice dislocations with Burgers vectors $\mathbf{b}=\frac{1}{2}\langle 110\rangle$. The dislocation grid spacing, d, conforms to Franck's equation,[10] or, equivalently, to the geometry of Bollmann's O lattice,[11] and is given by

$$d=\frac{|\mathbf{b}|}{2\sin(\theta/2)} . \tag{1}$$

As described, for example, by Brokman and Balluffi,[12] the atomic displacements in such boundaries consist, to a large extent, of local rotations around the O lattice elements in the Wigner-Seitz cells centered on the O lattice elements, as illustrated schematically for the $\Sigma 25(\theta=16.3°)$ boundary in Fig. 1. These relaxations occur in opposite directions in the two crystals facing the boundary, and tend to produce patches of perfect crystal centered on each O lattice element separated by localized screw dislocations (dashed lines in Fig. 1).

X-ray-diffraction observations[3,4,7–9] show that this general pattern of relaxation extends to higher angles up to, and including, the $\Sigma 5(\theta=36.9°)$ misorientation. In the latter boundary, the structure can no longer be well described in terms of discrete lattice dislocations. Nevertheless, the rotational pattern of relaxation persists. Brokman and Balluffi[12] have explained the main features of the observed distribution of scattered intensity from the series of boundaries on the basis of an approximate model in which the boundary displacement field is represented by low-order Fourier components that represent the rotational relaxation in a simple manner. In this model, the intensity from these Fourier components falls on the boundary diffraction lattice[1] (BDL)

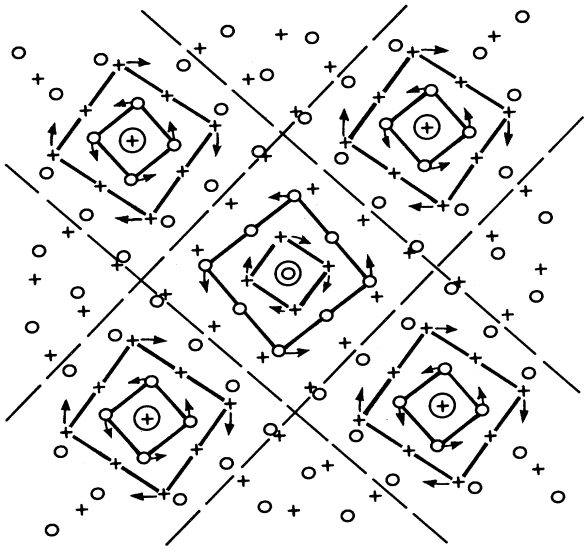

FIG. 1. Schematic diagram of "low-angle" $\Sigma 25(\theta = 16.2°)$ boundary showing rotational relaxations (indicated by arrows) that produce a square array of localized lattice screw dislocations. *O* lattice element (encircled) at center of each cell. Dashed lines indicate square array of dislocations. + and ○ indicate first planes of crystals 1 and 2 facing the boundary.

in satellite clusters which are centered on the various reflections from the perfect crystals 1 and 2, as is indeed observed. Computer simulations of the boundary structures using empirical pair potentials[9,13] also indicate that the rotational relaxation persists over the full range of misorientation between 0° and 36.9°. However, the magnitudes of the relaxations tend to decrease substantially as θ increases towards the $\Sigma 5$ misorientation and the screw dislocation spacings decrease.

In contrast to this, Fitzsimmons and Sass[3,4] have recently measured relative x-ray boundary structure factors for both the $\Sigma 13$ and $\Sigma 5$ boundaries, and have deduced models in which the rotational relaxation in the $\Sigma 5$ boundary is larger than for the lower-angle $\Sigma 13$ boundary, and is, in fact, also very much larger than that predicted by any of the computer-simulation calculations. This result has been surprising to workers in the field and has cast doubt on the usefulness of the pair-potential calculations. In an effort to explain this result without incurring unrealistically large atomic displacements, Oh and Vitek[14] proposed a structural model in which the $\Sigma 5$ boundary was assumed to possess "structural multiplicity," i.e., variants of the basic structural units which would make up the simple short-period $\Sigma 5$ boundary. However, this model possesses a number of *ad hoc* features and has remained unconvincing.

III. MEASUREMENTS OF STRUCTURE FACTORS FOR [001] TWIST BOUNDARIES

A. Specimens

The required thin-film bicrystal specimens [see Fig. 1 of paper I (Ref. 1)] were prepared by welding single-crystal gold films together at the desired misorientation according to the basic procedure first described in Ref. 15 and used subsequently to prepare all specimens used for boundary x-ray-diffraction studies.[3,4,7–9] (001) single-crystal films, 75 nm thick, were first prepared by epitaxial vapor deposition of gold on cleaved (001) NaCl single-crystal substrates held at 300 °C in a vacuum bell jar evacuated to 10^{-8} Torr. The films, while still on their substrates, were then welded together face-to-face at the desired twist angles in air at 250 °C at a pressure of ~10 psi using a specially designed press. The welded bicrystal was then held for 150 min at the welding temperature for purposes of annealing and then cooled back to room temperature. No intermediate silver "buffer" layer was used, as in Ref. 15, in order to avoid possible contamination with silver.

Next, the NaCl substrate was dissolved away from the thin-film bicrystal specimen, which was left floating in a shallow dish of water. The floating film was then picked up on a 7.6-μm-thick Kapton polymer film, which, in turn, was already stretched on a circular aluminum ring, which served as the specimen holder [see Fig. 7 of paper I (Ref. 1)] for mounting on the goniometer. With some practice, the picked-up bicrystal could be laid out on the stretched Kapton film and drained and dried in a very flat condition so that no wrinkling or bending could be detected by reflected light. In addition, the bicrystal remained securely attached to the film under all circumstances after this procedure.

After the diffraction measurements were concluded, the specimen was removed from the stretched film, and representative areas from all regions of the boundary were examined by transmission electron microscopy. A typical view of a $\Sigma 113$ boundary is shown in Fig. 2. Undesirable "extraneous" defects, inevitably present in all of the specimens prepared, are seen to be present. These include (1) bubbles (due to incomplete welding), (2) sets of edge dislocations with their Burger vectors normal to the

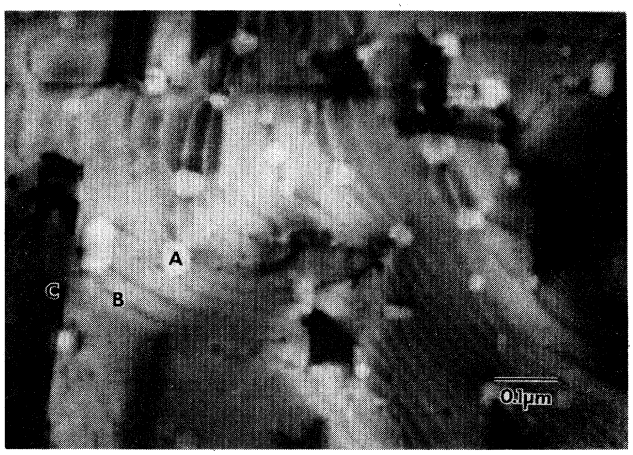

FIG. 2. Electron micrograph of typical grain-boundary area in $\Sigma 113$ specimen. Visible are bubbles (at *A*), dislocations with Burgers vectors normal to the boundary (at *B*), and impinging stacking faults or thin twins (at *C*).

boundary plane (due to the presence of small local tilt components), (3) variations in the spacings of the intrinsic screw dislocation network (due to small variations in the local twist angle caused by the presence of subgrains in crystals 1 and 2), and (4) thin twins or stacking faults which impinged on the boundary. We note that the fine intrinsic screw dislocation network is not visible in Fig. 2. Also, the thin twins or stacking faults lie in crystals 1 and 2 at an angle of 55° with respect to the boundary plane. Hence, each produces only a thin line defect along its trace in the boundary.

Considerable efforts were made in the specimen-preparation procedure to reduce the presence of these defects. Substrate NaCl crystals producing the sharpest x-ray-diffraction peaks were selected, and, after the cleaving was performed, care was taken to select the substrates having the flattest (001) surfaces with the minimum presence of cleavage steps. Also, the specimens were annealed after the welding operation to the maximum extent possible without causing the layered bicrystal configuration to convert to the more stable columnar grain structure illustrated, for example, in Fig. 1 of Tan *et al.*[16] We note the bicrystal thickness finally chosen represented a compromise between a specimen that was thick enough to withstand appreciable annealing, yet thin enough to produce an acceptably low background-scattering intensity near the grain-boundary diffraction peaks of interest. Finally, a considerable number ($\sim$15–20 for each Σ value) of specimens covering the desired range of Σ values was prepared using these procedures, and the specimens producing the sharpest and most intense grain-boundary diffraction peaks were selected for the final diffraction measurements. These final boundaries possessed twist angles that deviated from the ideal exact Σ misorientations by a few tenths of a degree in some cases. The actual deviations (see data in Tables I and II) were as follows: −0.2° (for Σ113) 0.0° (for Σ25), 0.0° (for Σ13), 0.0° (for Σ17), and 0.4° (for Σ5). As demonstrated in Ref. 17, and as verified by our experimental results, these deviations could not have affected our analysis significantly, and we shall therefore refer to our boundaries as "Σ113, Σ25, Σ13, Σ17, and Σ5 boundaries" throughout.

Upon completion of the diffraction measurements, the fraction of the boundary area in each specimen intercepted by bubbles (e.g., Fig. 2) was carefully measured by transmission electron microscopy by lineal analysis. The values were found to lie in the range 0.6–0.8 and were used as correction factors in the calculation of the final structure factors in order to account for the missing grain-boundary areas. As a final check on the entire procedure, it was verified that reproducible results (within the final estimated ranges of error described below) were obtained for specimens of the same Σ value.

It is believed that any systematic errors in our integrated intensity measurements caused by the defects described above also fell within the final estimated ranges of error described below. The effects of the bubbles were accurately accounted for as just described. The cores of the edge dislocation and the traces of the thin twins (or stacking faults) constituted narrow line defects that affected only a very small fraction of the boundary area. They therefore should have scattered relatively little intensity out of the boundary diffraction peaks into regions of reciprocal space where it was not counted. Also, the crystal mosaic and long-range dislocation strain fields undoubtedly caused some broadening of the grain-boundary diffraction peaks. However, most of this intensity must have been included in the integrated intensity measurements as described below.

B. Diffraction measurements and results

Integrated intensity measurements for various grain-boundary reflections on the BDL and also for nearby crystals-1 and -2 reflections were measured in different regions of reciprocal space for the different boundaries using the scanning methods described in paper I.[1] A typical relatively strong grain-boundary peak produced by one of these scans is shown in Fig. 3. A diagram showing the reflections which were measured in the $L=0$ plane of the BDL of the Σ113 boundary is shown in Fig. 4. We note that the BDL indices of the crystal-1 lattice reflections for all boundaries in the series are given by

$$H = rh/2 - sk/2 ,$$
$$K = sh/2 + rk/2 , \qquad (2)$$
$$L = l ,$$

where (hkl) are the lattice reflection indices (referred to the reciprocal lattice of crystal 1), and r and s are integers given by $(r,s)=(15,1)$ for Σ113, (7,1) for Σ25, (5,1) for Σ13, (5,3) for Σ17, and (3,1) for Σ5. The corresponding indices for crystal 2 may be easily derived on the basis of symmetry. Absolute static boundary structure factors, $|F_b^0|$, were then determined from the integrated intensity data using Eqs. (16)–(18) of paper I.[1] The required correction factor, Γ, was evaluated as will be explained in

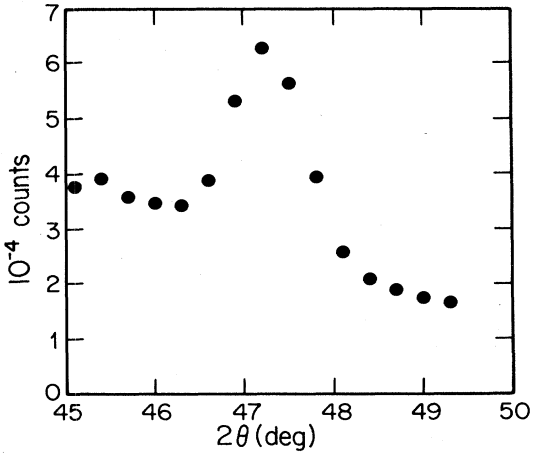

FIG. 3. Typical scan of relatively strong grain-boundary diffraction peak. (16,0,0) peak for Σ113 boundary. Error bars fall within the solid circles.

TABLE I. Measured and calculated absolute static structure factors squared, $|F_b^0|^2$, for Σ113, Σ25, Σ13, and Σ17 boundaries.

Boundary	H,K,L	Nearest lattice reflection (hkl)	$\|F_b^0\|^2_{\text{meas}}$	$\|F_b^0\|^{2a}_{\text{calc}}$
Σ113	12,0,0	200	300±240	75
(θ=7.4°)	14,2,0	200	30 000±7600	22 000
	12,2,0	200	150±100	99
	13,1,0	200	2000±1000	1700
	14,0,0	200	90 000±18 000	100 000
	14,−2,0	200	26 000±6600	22 000
	16,0,0	200	100 000±21 000	100 000
	17,1,0	200	2400±800	2400
	18,0,0	200	370±150	130
	17,3,0	200	610±250	1000
	18,2,0	200	200±100	380
	19,11,0	220	3300±1500	1500
	17,13,0	220	39 000±10 000	59 000
	16,12,0	220	0±100	36
	17,15,0	220	200±150	500
	15,13,0	220	0±150	260
	18,14,0	220	360±180	27
	18,12,0	220	5700±2000	7000
	17,11,0	220	310±120	38
	16,16,0	220	590±270	380
	15,15,0	220	460 000±100 000	420 000
	14,14,0	220	700±350	310
	28,0,0	400	2300±900	3200
	26,4,0	400	0±150	590
	27,3,0	400	4000±1500	2600
	28,2,0	400	16 000±4700	12 000
	29,1,0	400	76 000±34 000	59 000
	30,0,0	400	91 000±18 000	90 000
	28,4,0	400	9500±6600	3600
	29,3,0	400	31 000±15 000	43 000
	31,1,0	400	78 000±23 000	51 000
	31,3,0	400	16 000±8000	22 000
	32,2,0	400	7900±2800	7100
	8,9,1	111	0±100	65
	25,10,1	311	950±470	1100
	9,24,1	311	4500±1800	6100
	6,25,1	311	2400±840	2900
	7,24,1	311	16 000±4000	20 000
	4,21,1	311	1700±700	950
	5,22,1	311	17 000±5000	17 000
	10,21,1	311	42 000±15 000	56 000
	5,24,1	311	50 000±18 000	41 000
	7,22,1	311	120 000±42 000	150 000
	8,21,1	311	12 000±4000	18 000
	9,20,1	311	3700±1300	3300
	6,21,1	311	3700±1300	4700
	16,0,4	204	63 000±19 000	69 000
Σ25	6,2,0	200	200±70	190
(θ=16.3°)	6,0,0	200	870±440	530
	8,0,0	200	770±190	830
	8,2,0	200	100±40	87
	14,0,0	400	710±210	400
	13,1,0	400	290±90	410
	9,5,0	220	530±190	470
	7,7,0	220	3500±1200	2800
Σ13	5,3,0	220	1.8±1.8	1
(θ=22.6°)	5,5,0	220	170±60	230
	4,0,0	200	26±9	36

TABLE I. (*Continued*).

Boundary	*H,K,L*	Nearest lattice reflection (*hkl*)	$\lvert F_b^0\rvert^2_{\text{meas}}$	$\lvert F_b^0\rvert^{2\text{a}}_{\text{calc}}$
	6,0,0	200	85±21	89
Σ17	8,0,0	220	170±70	190
(θ=28.1°)	9,3,0	220	13±8	0
	3,3,0	200	71±25	23
	5,5,0	200	79±20	87

[a]Calculated using embedded-atom model.

detail in Sec. IV B. All other required quantities in Eq. (16) of paper I were either known or obtained from appropriate measurements. A listing of all measured structure factors squared corresponding to integer values of *H*, *K*, and *L* is given in Tables I and II. In addition, these quantities in the $L=0$ plane are displayed in Figs. 5–8 for the Σ113 boundary in the vicinity of the (400) lattice reflection and for the Σ25, Σ13, Σ17, and Σ5 boundaries. As may be seen, measurements were made in the $L=0$, 1, and 4 layers of the BDL in regions close to (200), (220), (400), (111), (311), (204), and (402) lattice reflections. The error limits given are estimates based mainly on the uncertainties which were involved in separating the grain-boundary diffraction peaks from the background. This was due to the fact that a relatively high background was present in the low-resolution diffractometry technique employed [see paper I (Ref. 1)]. The errors were determined by extrapolating the background intensity into the peak regions in various reasonable ways in order to estimate the background, and by finding the variations in integrated intensity resulting from the different choices. The other sources of error, such as errors in counting, were generally relatively small. Finally, $\lvert F_b^0\rvert^2$ was also measured as a function of *L* along several relrods[1] corresponding to relatively strong boundary reflections, as shown in Figs. 9 and 10.

The results show that the magnitudes of the measured values of $\lvert F_b^0\rvert^2$ ranged over about 6 orders of magnitude and decreased generally in the order Σ113→Σ25→Σ13→Σ17→Σ5, which is also in the order of continuously increasing twist angle. This decrease with increasing twist angle could be shown more systematically by considering the scattered power from boundary reflections, which maintained fixed positions relative to lattice reflections over the entire series of boundaries studied. Two of these boundary reflections are shown at *A* and *B* in Fig. 4 for the particular case of the Σ113 boundary. The reflection at *A* for the Σ113 boundary, and for all the other boundaries as well, was always located on the *H* axis between the two (200) lattice reflections at the relative position shown, while the *B* reflection was always midway between the two (220) lattice reflections. In general, the scattering power from unit area of the grain boundary should depend on the boundary structure through the quantity $\lvert n_b F_b^0\rvert^2$; n_b is the number of boundary unit cells per unit area of bound-

TABLE II. Measured and calculated absolute static structure factors squared, $\lvert F_b^0\rvert^2$, for Σ5 boundary.

Boundary	*H,K,L*	Nearest lattice reflection (*hkl*)	$\lvert F_b^0\rvert^2_{\text{meas}}$	$\lvert F_b^0\rvert^{2\text{a}}_{\text{calc}}$	$\lvert F_b^0\rvert^{2\text{b}}$	$\lvert F_b^0\rvert^{2\text{c}}$
Σ5	4,0,0	200	4.7±1.6	3.0	2.98	164.2
(θ=37.3°)	2,2,0	200	2.2±1.1	1.7	2.93	59.7
	4,1,0	200	0.7±0.4	0.9	0.57	4.9
	2,0,0	200	1.0±0.6	0.3	1.01	31.8
	3,2,0	200	0.0±0.1	0.2	0.09	2.9
	1,1,0	200	0.0±0.2	0.0	0.02	0.1
	3,0,0	200	0.0±0.1	0.0	0.00	0.0
	1,0,0	200	0.0±0.1	0.0	0.00	0.0
	3,3,0	220	6.3±2.2	3.7	7.34	136.9
	5,2,0	220	0.0±0.3	0.3	0.31	3.4
	6,1,0	400	1.3±0.9	1.7	1.36	15.9
	7,0,0	400	0.0±0.2	0.0	0.00	0.0
	4,4,0	420	1.3±0.6	0.1	0.68	84.5
	5,4,0	420	1.8±0.9	1.9	1.53	25.5

[a]Calculated using embedded-atom model.
[b]Calculated using minimum-*R* search method (see text).
[c]Calculated from the model of Fitzsimmons and Sass (Ref. 4).

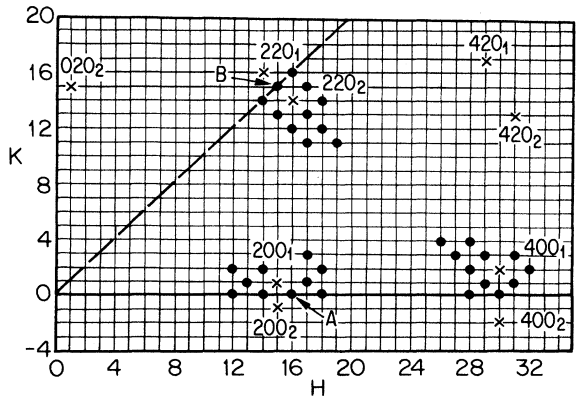

FIG. 4. $L=0$ plane of BDL for $\Sigma 113$ boundary. Solid circles indicate reflections which were measured (see Table I). ×'s indicate lattice reflections.

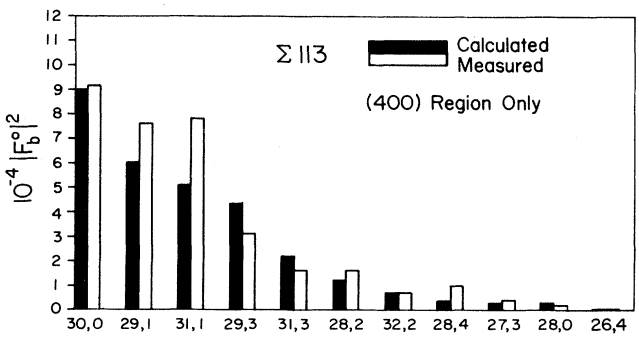

FIG. 5. Display of measured and calculated (embedded-atom model) static structure factors squared for $\Sigma 113$ boundary near (400) lattice reflection.

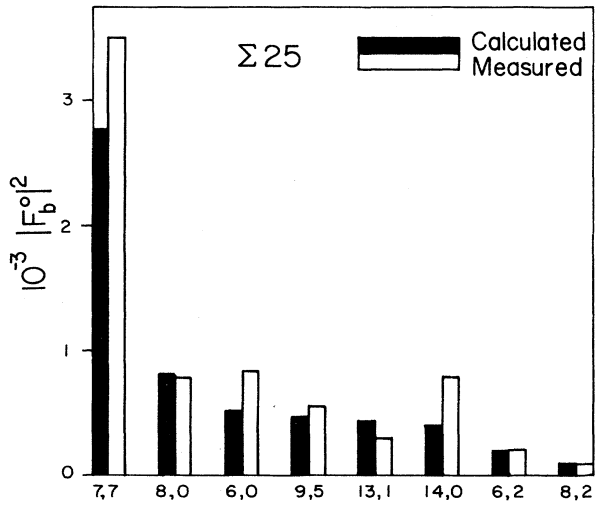

FIG. 6. Display of measured and calculated (embedded-atom model) static structure factors squared for $\Sigma 25$ boundary.

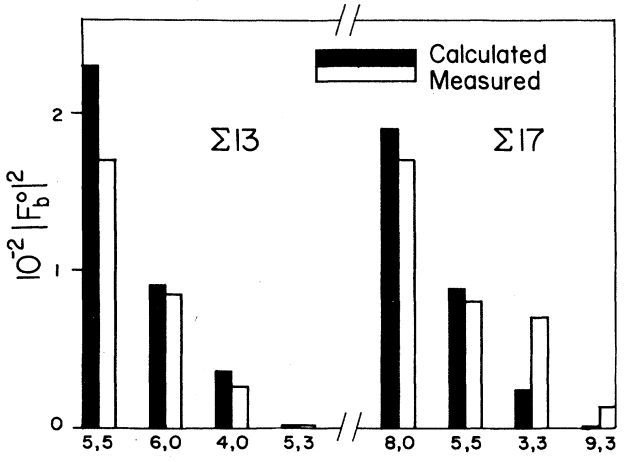

FIG. 7. Display of measured and calculated (embedded-atom model) static structure factors squared for $\Sigma 13$ and $\Sigma 17$ boundaries.

ary. In the present series of boundaries, $n_b^2=4/a^4\Sigma^2$, where a is the lattice parameter, and therefore, the scattering power per unit area should be proportional to the quantity $|F_b^0|^2/\Sigma^2$. This quantity, for the boundary

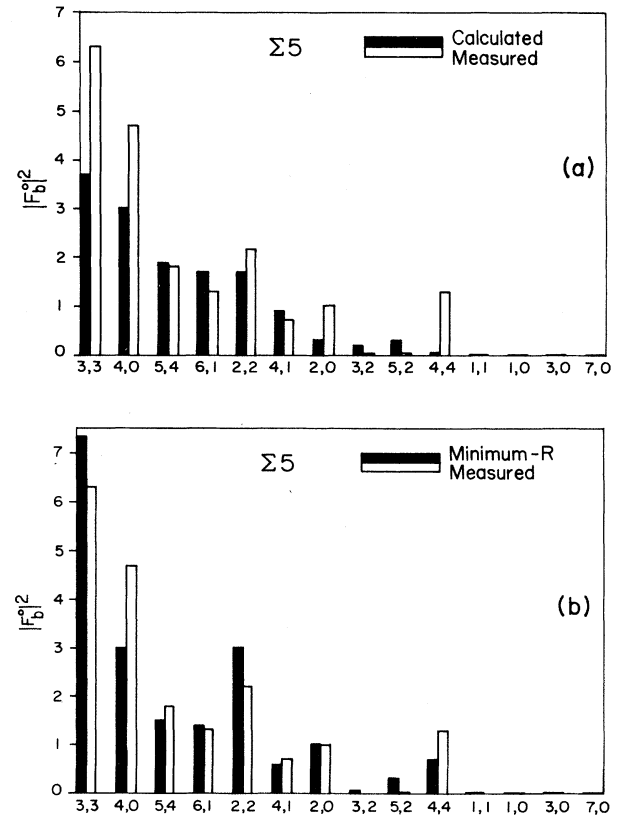

FIG. 8. Display of static structure factors squared for $\Sigma 5$ boundary. (a) Measured values and calculated values using embedded-atom model. (b) Measured values and values obtained for minimum-R structure.

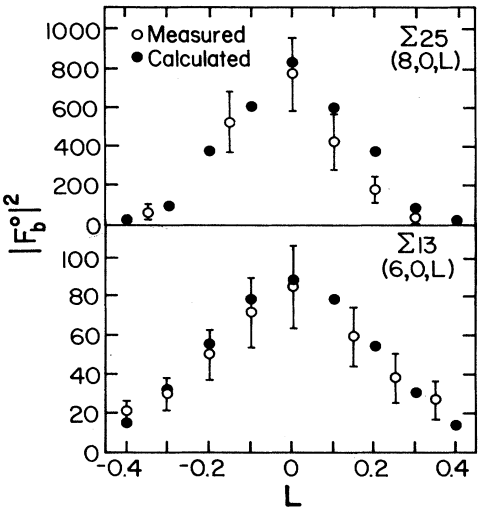

FIG. 9. Measured and calculated (embedded-atom model) values of $|F_b^0|^2$ as a function of L along relrods for Σ25 and Σ13 boundaries.

reflections at the A and B positions, was therefore plotted versus θ for the various boundaries, as shown in Figs. 11 and 12, respectively. The results show that the scattering power per unit area, as measured by $|F_b^0|^2/\Sigma^2$, decreased in a remarkably regular manner with increasing θ.

The relrod scans in Figs. 9 and 10 possessed maxima at $L=0$, and full widths at half maximum (FWHM's) which increased with increasing reciprocal O lattice spacing, $1/d$, as shown in Fig. 13. Also, as may be seen, the magnitudes of the FWHM's and the values of $1/d$ agreed within about 30%.

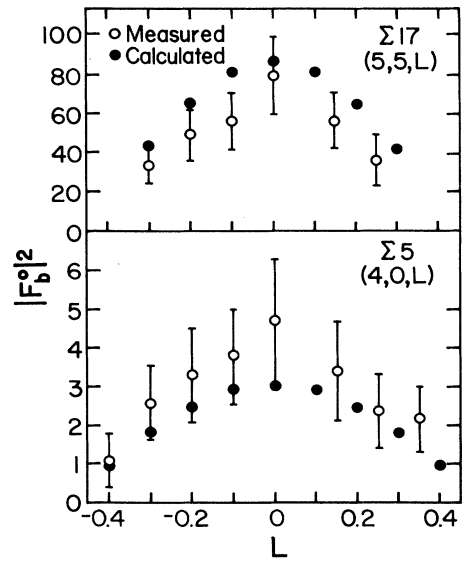

FIG. 10. Measured and calculated (embedded-atom model) values of $|F_b^0|^2$ as a function of L along relrods for Σ17 and Σ5 boundaries.

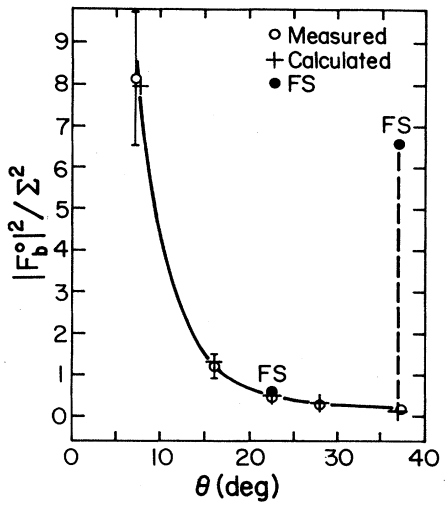

FIG. 11. Measured and calculated (embedded-atom model) values of the quantity $|F_b^0|^2/\Sigma^2$ (a measure of the scattering power per unit area of boundary) plotted as a function of θ for the present series of boundaries. Also shown are values predicted by the models of Fitzsimmons and Sass (FS) for the Σ13($\theta=22.6°$) (Ref. 3) and Σ5($\theta=36.9°$) (Ref. 4) boundaries. All values are for the "A reflection" shown in Fig. 4 for the special case of the Σ113 boundary. Error bars fall within the symbols for $\theta > 20°$.

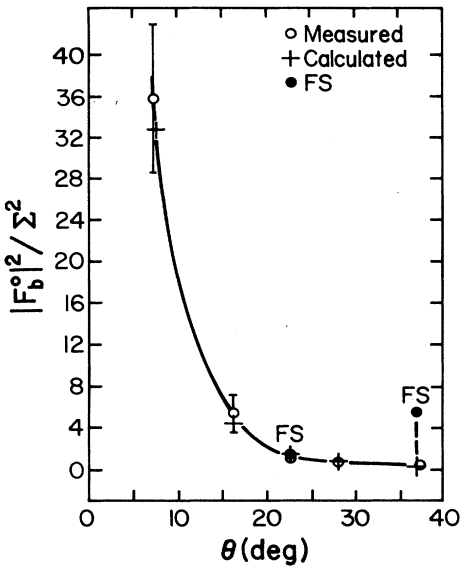

FIG. 12. Measured and calculated (embedded-atom model) values of the quantity $|F_b^0|^2/\Sigma^2$ (a measure of the scattering power per unit area of boundary) plotted as a function of θ for the present series of boundaries. Also shown are values predicted by the models of Fitzsimmons and Sass (FS) for the Σ13($\theta=22.6°$) (Ref. 3) and Σ5($\theta=36.9°$) (Ref. 4) boundaries. All values are for the "B reflection" shown in Fig. 4 for the special case of the Σ113 boundary. Error bars fall within the symbols for $\theta > 20°$.

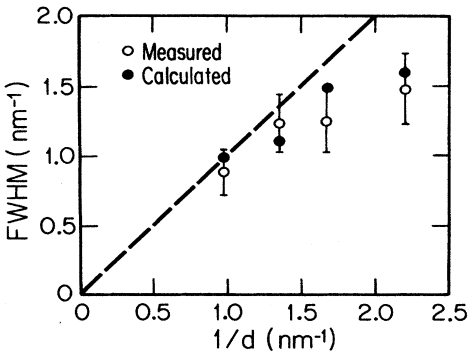

FIG. 13. Full width at half maximum (FWHM) of relrod peaks shown in Figs. 9 and 10 for Σ25, Σ13, Σ17, and Σ5 boundaries as a function of reciprocal O lattice spacing, $1/d$.

IV. CALCULATION OF BOUNDARY STRUCTURE FACTORS USING THE EMBEDDED-ATOM MODEL

A. Computational method

To calculate grain-boundary structure factors, the equilibrium atomic structure of the boundary must first be determined using a model for the interatomic interactions and for the thermodynamic environment. While *ab initio* molecular-dynamics calculations[18] of boundary structure are now possible, they remain computationally demanding and therefore are limited to short-period geometries. Many of the previous grain-boundary calculations[13] have relied on the empirical pair-potential model. The simplicity of this model makes it attractive, but when applied to metallic systems it can suffer from serious physical deficiencies that are principally related to difficulties in dealing with the volume-dependent contributions to the total energy. These contributions simulate the cohesive energy of the electron gas and describe the elastic properties of the metal. Constant-volume calculations have been employed in an effort to circumvent this problem, but they remain unsatisfactory since the local grain-boundary volume is likely to be different from that of the bulk. In addition, the constant-volume constraint excludes any realistic thermodynamic treatment of the grain-boundary core region and adjoining lattices. In the present paper we have chosen the empirical embedded-atom method[2] to model the grain-boundary structure since it avoids the physical limitations of a pair-potential method, and also the practical computational limitations of a formal quantum-mechanical approach. When coupled with molecular dynamics or statics, it provides an efficient method for simulating the microscopic properties of grain boundaries.

The basis of the embedded-atom model may be summarized as follows. The total energy of an assembly of atoms is decomposed into a sum of short-range pair-potential interactions plus a sum of embedding energies. An embedding energy is the energy required to place an atom into the background electron density of the surrounding atoms. For simplicity, this electron density is computed as the superposition of the atomic electron densities. The embedding function and pair-potential function are determined empirically by fitting to various bulk and point-defect properties of the metal—gold in our case. Since the embedding energy is a function of the electron density, volume-dependent contributions to the computed grain-boundary energy are determined more accurately than if pair potentials alone were used. As a consequence, volume changes at the boundary are also expected to be correspondingly more accurate. The method has achieved considerable success in simulating a wide range of defects in a numer of fcc metals and alloys.[19–24] The reason for this success can be attributed, in part, to the physical similarity of the method to more fundamental approaches based on density-functional theory,[25] effective-medium theory,[26,27] and tight-binding theory.[28]

The computational cells used in the calculations were rectangular blocks of atoms with cross sections defined by the appropriate CSL unit cells. Thus, for example, the cell for the Σ113 twist boundary had faces parallel to (001), (15,$\bar{1}$,0), and (1,15,0). [001] twist boundaries were introduced into the cells, without changing their shape, by displacing non-CSL sites on one side of the boundary that is located at the midplane of the cell. Periodic border conditions were applied, both in the boundary plane and normal to it, thereby introducing a second twist boundary into the cell. To miminize the interaction between the two twist boundaries, which are symmetrically equivalent and separated by half a cell length, the [001] block dimension was maximized. In the results that follow, this dimension was taken to be 80 (002) planes for all the CSL boundaries calculated. Thus, in determining the twist boundary structure factors, only the 20 (002) planes on either side of a given boundary were considered. In the case of the Σ5 and Σ13 boundaries, four CSL unit cells were used in the plane of the boundary to avoid effects due to the range of the potential, and, therefore, the total number of atoms contained in the computational cell ranged from 800 to 4520 atoms. The embedding function for gold was used,[29] and no attempt was made to modify it to improve the fit to the present x-ray observations.

All five of the CSL boundaries studied (Σ5, Σ13, Σ17, Σ25, and Σ113) were relaxed statically using a conjugate gradient algorithm in a constant- (zero-) pressure simulation to reduce all the atomic forces to less than 10^{-4} eV/Å. Having the atomistic structures, the geometrical grain-boundary structure factor, defined by

$$F_b(H,K,L)=\sum_{n=1}^{N}\exp[2\pi i(Hx_n+Ky_n+Lz_n)]\ , \qquad (3)$$

where $x_n y_n, z_n$ are the fractional coordinates of the nth atom in the diffracting unit cell containing N atoms, was then determined for each of the five statically relaxed structures.

The statically determined structures of the Σ5 and Σ13 boundaries were used as initial configurations for a limited series of additional molecular-dynamics calculations. In these calculations, as with those performed statically, flexible borders were employed so that the computational

cell size and shape could change. The atomic velocities were rescaled to maintain a constant temperature of 300 K, and the simulations proceeded under hydrostatic pressure. The duration of the simulation for the Σ113 boundary was 11 700 time steps (11.7 ps or 265 Debye periods) and that for the Σ5 boundary was 3200 steps (3.2 ps or 72 Debye periods) with averages taken after 2000 steps. In the case of the Σ5 boundary, the model cross section in the boundary plane was increased to 100 CSL unit cells so that possible effects due to structural multiplicity[14] or boundary roughening[30] could be observed. As a consequence, the [001] block dimension for this calculation was reduced, so that the total number of atoms equaled 10 000. The instantaneous structure factor was computed every tenth time step after the 2000th time step, and an average over the duration of the simulation was determined. A molecular-dynamics simulation of a single crystal was also performed, so that an average dynamic value of $|F_c|^2_{\text{calc}}$ could be obtained under the same simulation conditions as those used for the grain boundaries.

B. Computational results

In order to find minimum-energy boundary structures, several test were made, involving both different translational states and the addition of structural unit variants. Rigid-body translations of crystal 2 with respect to crystal 1 in directions parallel to the boundary are possible for all the twist boundaries studied, but they have potentially the largest effect at the Σ5 boundary since it has the largest DSC lattice[11] unit cell. Therefore, a systematic study of translation states was only made for the Σ5 boundary, where it was found that the "CSL" state (in the notation of Bristowe and Crocker[13]) had the lowest energy. Higher in energy, by only a few percent, were the "types 1 and 2" translated structures.[13] In previous computer-simulation studies of the Σ5 boundary,[14,30] additional structural unit variants of the "CSL" state were found, involving large rotational displacement. These structures, called $A_1(A_2)$ and $B_1(B_2)$, were found to be unstable in the present study. The instability of the A and B structures was confirmed in the molecular-dynamics calculations of the Σ5 boundary where, during the simulation time scale, they were not observed to form. About 10% of the CSL units in this calculation did, however, migrate normal to the boundary by one (002) interplanar spacing. Upon quenching, this roughened boundary structure remained stable, but the roughening had no significant observable effect on the computed $(H,K,0)$ structure factors presented in Table II. The structural model for the Σ5 boundary proposed by Fitzsimmons and Sass[4] was also used as a starting configuration in the calculation, and was found to be unstable having an energy about 7 times that of the minimum-energy "CSL" state. This agrees with a previous pair-potential calculation of a similar model proposed by Budai *et al.*[9]

Maps of the computed displacement vectors [projected on the (001) boundary plane] of the atoms in the first two planes of crystals 1 and 2 facing the boundary midplane are shown in Fig. 14 for the five boundaries. In these maps, the arrows, which are enlarged by a factor of 3,

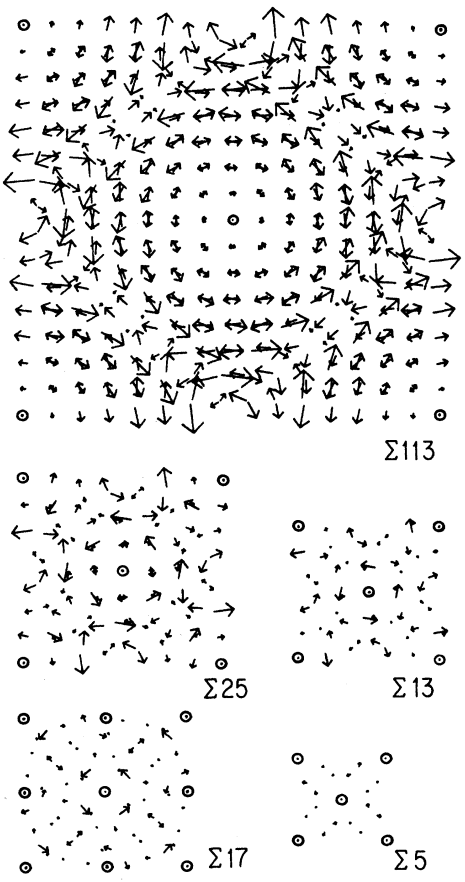

FIG. 14. Calculated (static embedded-atom model) displacement fields projected onto (001) boundary plane. Vectors point from the unrelaxed geometrical configuration to the relaxed equilibrium state, and are magnified by a factor of 3. Only atomic displacements in the first two planes on either of the boundaries are shown.

point from the unrelaxed geometrical configuration to the relaxed configuration. Each structure occupies the "CSL" translational state. Figure 15 shows the computed magnitudes of the largest displacement vectors [projected on the (001) boundary plane] for each twist boundary. Since the Σ5 and Σ13 boundaries were of special interest (see below), information describing the detailed coordinates of the significantly displaced atoms in these boundaries is given in Table III and Fig. 16. Figure 16 identifies the irreducible set of atoms in each boundary whose positions must be specified. As pointed out in Refs. 3, 4, and 9, the positions of all the other atoms in the CSL translational state are symmetry related. It is noted that many of the computed displacements, especially those in the boundary plane, are not significantly different from those determined using typical pair potentials.[9,13] Displacements normal to the boundary, however, may exhibit subtle differences that will be reflected in the detailed shape of the relrod profiles along L. In fact, further results, to be published elsewhere, indicate that the embedded-atom model accurately reproduces many profile details, such as subsidiary maxima, that are not

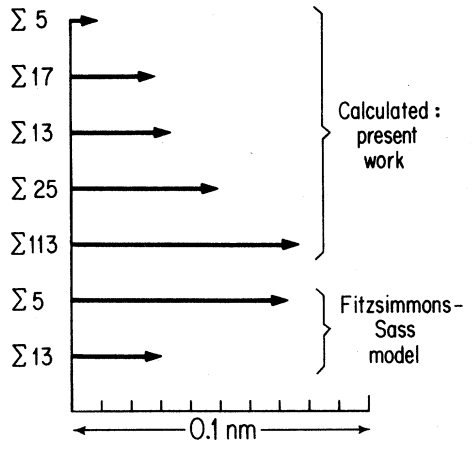

FIG. 15. Magnitudes of the largest displacement vectors projected onto the (001) boundary plane for the present boundary structures calculated with the static embedded-atom model and for the Fitzsimmons-Sass models (Refs. 3 and 4).

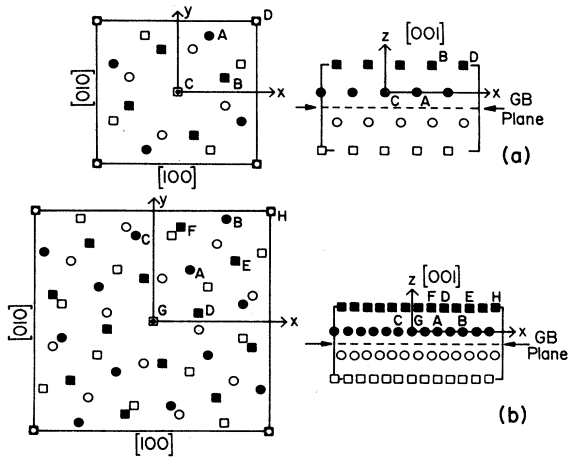

FIG. 16. Maps showing irreducible set of atoms in unrelaxed structures of boundaries in CSL translational state (a) Σ5. (b) Σ13.

found in pair-potential calculations.

The calculated structure factors squared, $|F_b^0|^2$, for the entire series of static boundary structures are listed in Tables I and II and displayed in Figs. 5–12 for comparison with the corresponding measured values. Not shown in Figs. 11 and 12 are additional calculated points for the Σ61, Σ41, Σ73, Σ53, and Σ29 boundaries, which are all very close to the curves shown.

As already mentioned, the measured static structure factors just discussed were derived from the experimental data through use of a Debye-Waller difference-factor correction, Γ, given by Eq. (18) of paper I.[1] It was argued there that this factor is close to unity and can be estimated to a degree of accuracy sufficient for present purposes. The values of the mean-squared atomic displacements, $\langle u_b^2 \rangle$, in units of nm^2, required for calculating Γ for the series of boundaries in the present work were taken as follows: 9.5×10^{-5} (Σ113), 10.1×10^{-5} (Σ25), and 10.4×10^{-5} (for Σ13, Σ17, and Σ5). Also, $\langle u_c^2 \rangle = 8.0\times10^{-5}$.[31] The value 10.4×10^{-5} for all three high-angle boundaries is intermediate between the value for the Σ13 boundary estimated by Fitzsimmons, Burkel, and Sass[31]

TABLE III. Atomic displacements in Σ5 and Σ13 boundaries.

	Atom[a]	Δx (nm)[a]	Δy(nm)[a]	Δz (nm)[a]
		Σ5		
3D Structure	*A*	0.0024	0.0085	0.0182
calculated using	*B*	−0.0031	−0.0014	0.0123
embedded-atom model	*C*	0.0	0.0	−0.0031
	D	0.0	0.0	−0.0190
		Σ13		
	A	0.0169	−0.0042	0.0123
	B	−0.0060	0.0323	−0.0018
	C	0.0207	−0.0080	0.0198
	D	−0.0019	−0.0057	0.0129
	E	−0.0013	0.0028	0.0126
	F	0.0065	0.0034	0.0127
	G	0.0	0.0	0.0021
	H	0.0	0.0	0.0004
		Σ5		
Projected structure	*A*	0.0	0.0105	
yielding	*B*	−0.0008	−0.0040	
minimum *R* factor	*C*	0.0	0.0	
	D	0.0	0.0	

[a]See Fig. 16.

from widely scattered experimental data and the value calculated recently by Sutton.[32] The lower values for the $\Sigma 113$ and $\Sigma 25$ boundaries were chosen to be consistent with the expectation that $\langle u_b^2 \rangle$ should progressively decrease with decreasing angle in the low-angle regime. This expectation is based on the fact that an increasingly large fraction of the scattering from low-angle boundaries arises from the only slightly strained bulk lattice, which is outside the distorted material in the primary dislocation cores as the twist angle decreases. The value of $\langle u^2 \rangle$ in this slightly strained region should be close to that of the perfect bulk lattice. Use of these values produced values of Γ in the range $0.9 < \Gamma \leq 1.25$.

We note, finally, that the molecular-dynamics calculations performed for the $\Sigma 113$ boundary yielded values of $\Gamma = |F_b^0|^2 |F_c|^2 / |F_c^0|^2 |F_b|^2$ for all strong and medium-strength reflections for which there were observations. It was found that this ratio for the majority of the values could deviate from unity by up to 20%, depending on the diffraction vector. However, in a few apparently anomalous cases, larger deviations were computed, as well as negative ones, suggesting that the simulation time scale was probably too short to obtain accurate dynamical structure factors. Because of this problem and the prohibitively long computing times required, the dynamical calculations were eventually abandoned.

V. ANALYSIS AND DISCUSSION OF RESULTS

A comparison of the measured and calculated structure-factor data presented in Tables I and II and in Figs. 5–12 shows general agreement (within estimated experimental error) between measured and calculated values of $|F_b^0|^2$ for the strong and medium reflections. For the weaker reflections, larger discrepancies are present in a number of cases, and this may be attributed to relatively large uncertainties in estimating errors in the weak cases. This agreement is consistent with the boundaries being in the CSL translational state, which concurs with the previous conclusion of Fitzsimmons and Sass[3,4] for the $\Sigma 5$ and $\Sigma 13$ boundaries. In particular, we find $|F_b^0|^2 = 0$ for the (100), (300), and (700) reflections for the $\Sigma 5$ boundary, in compliance with the selection rules for the CSL translational state.[3,4,9]

The general forms of both the measured and calculated scattering results appearing in Figs. 5–13 are readily understood on the basis of the main features of the calculated boundary structures shown in Figs. 14 and 15. The calculated relaxations in Fig. 14 have predominant rotational components around the *O* lattice elements, in agreement with the discussion in Sec. II and the schematic diagram in Fig. 1. The displacement fields corresponding to these rotations are therefore expected to extend into crystals 1 and 2 adjoining the boundary a distance approximately equal to the *O* lattice spacing, d. The boundary "thickness" is then approximately d. The full width at half maximum of the diffraction relrods shown in Fig. 13 should then be about equal to $1/d$, as is indeed the case.

The magnitudes of the calculated relaxations are seen to decrease monotonically with increasing θ, as shown in Figs. 14 and 15, and reach quite small values for the $\Sigma 5$ boundary. This should cause a corresponding monotonic decrease in the scattered intensity per unit area of grain boundary, as is verified in Figs. 11 and 12. A simple intuitive interpretation of this result may be given in terms of the dislocation model for [001] twist boundaries described in Sec. II. At small twist angles, the screw dislocations are far apart and highly localized. Hence, large relaxational displacements are present over relatively large volumes of material, such as, for example, for the $\Sigma 113$ boundary in Fig. 14. As θ increases, the dislocation spacing decreases until eventually the dislocation cores overlap. At this point, the dislocations are no longer discrete and localized, and the displacements associated with them are greatly reduced. In addition, the thickness of the displacement field is drastically reduced. These factors then combine to produce a relatively weak boundary scattering.

The overall degree of agreement between the measured and calculated structure factors for each boundary may be examined on a more quantitative basis by evaluating the R factor:

$$R = \left[\sum_i (|F_b^0|_{i,\text{meas}} - |F_b^0|_{i,\text{calc}})^2 \Big/ \sum_i |F_b^0|_{i,\text{meas}}^2 \right]^{1/2} . \quad (4)$$

This residual is essentially a least-squares fit of the observed data to the calculated structure and is used in conventional crystal-structure analysis as a parameter that is minimized with respect to the location of atoms within a trial structure.[33] Other similar forms of the residual have been used previously, including the χ^2 parameter employed by Fitzsimmons and Sass.[3,4] All residuals involve a sum of relative discrepancies between the observed and calculated structure factors. Care is needed in the interpretation of R, since, at best, it is a measure of how well the model structure has been fitted to the experimental data, and not necessarily how accurate the derived structure actually is. Although values of R less than 0.1 are usually considered to indicate a good correlation between a proposed structure and the observations for usual three-dimensional bulk diffractometry, higher values may be expected for grain-boundary structures because of the generally poorer signal-to-noise ratios and larger experimental errors. We also note that normalization of the structure factors will lead to different values of R, depending on the choice of the reference reflection. Although the use of relative structure factors may not be important if there are many observations, it may be critical if the data are sparse. Normalizing the structure factors to one particular reflection places in artificial condition on the evaluation of R that is not present if absolute structure factors are used. To avoid possible misinterpretation of the observed data, absolute structure factors have been used in the present study for the evaluation of R. Using the embedded-atom–calculated structures, the following R factors were computed: 0.11 ($\Sigma 113$), 0.15 ($\Sigma 25$), 0.15 ($\Sigma 13$), 0.28 ($\Sigma 17$), and 0.31 ($\Sigma 5$). The value of R for the $\Sigma 113$ boundary is almost certainly the most precise since for this boundary the reflections were

strongest, and the most data of high quality were collected. Its low value implies good agreement with the calculations. The relatively larger values of R, particularly for the $\Sigma 17$ and $\Sigma 5$ boundaries, indicate a lesser degree of agreement with the limited number of observations, as discussed further below.

Because of the controversial situation regarding the structure of the $\Sigma 5$ boundary discussed in Sec. II, more data were collected for this boundary than for the $\Sigma 17$, $\Sigma 13$, and $\Sigma 25$ boundaries. This allowed a further test of the goodness of fit between the observed and calculated results in the form of a standard electron-density difference map. This map is the difference between a Fourier synthesis of the electron-density distribution derived from the observed structure factors and from the calculated structure factors.[33] If the observed and calculated structure factors match exactly, the difference map has a flat topography. If the observations and calculations differ slightly, then characteristic minima and maxima appear, indicating that the calculated structure requires modification. One advantage of computing a difference map is that series-termination errors in the Fourier synthesis approximately cancel when the observations and calculations almost match. The electron density at a point (x,y,z) in the unit cell of the calculated structure may be computed accurately according to

$$\rho_{\text{calc}}(x,y,z)=\frac{1}{V}\sum_H\sum_K\sum_L F^0(H,K,L)_{\text{calc}}\exp[-2\pi i(Hx+Ky+Lz)]\ , \tag{5}$$

where V is the volume of the unit cell, and the summations extend (ideally) over all reciprocal space. (In practice, of course, the summations can only be performed over values of H,K,L for which there are observations.)

The corresponding expression for the electron density derived from the observations is impossible to evaluate precisely, since only the structure-factor amplitudes and not the phase angles are known from the measurements. It is therefore usual practice to evaluate the observed electron-density distribution approximately by using the phases of the calculated structure factors. Thus,

$$\rho_{\text{meas}}(x,y,z)=\frac{1}{V}\sum_H\sum_K\sum_L |F^0(H,K,L)|_{\text{meas}}\frac{F^0(H,K,L)_{\text{calc}}}{|F^0(H,K,L)|_{\text{calc}}}\exp[-2\pi i(Hx+Ky+Lz)]\ . \tag{6}$$

For [001] twist boundaries, it is the projection of the electron density onto the (001) boundary plane that is of most interest and requires only $(H,L,0)$ reflections for evaluation. Utilizing the conjugate symmetry of the structure factor and the plane group symmetry of the diffracting CSL unit cell, Eqs. (5) and (6) reduce to

$$\rho_{\text{calc}}(x,y)=\frac{1}{S}\sum_H\sum_K F^0(H,K)_{\text{calc}}\cos 2\pi(Hx+Ky)\ , \tag{7}$$

$$\rho_{\text{meas}}(x,y)=\frac{1}{S}\sum_H\sum_K |F^0(H,K)|_{\text{meas}}\frac{F^0(H,K)_{\text{calc}}}{|F^0(H,K)|_{\text{calc}}}\cos 2\pi(Hx+Ky)\ , \tag{8}$$

where S is the cross-sectional area of the unit cell. Thus, the electron-density difference synthesis is given by

$$\rho_{\text{diff}}(x,y)=\frac{1}{S}\sum_H\sum_K\left[\frac{F^0_{\text{calc}}(|F^0|_{\text{meas}}-|F^0|_{\text{calc}})}{|F^0|_{\text{calc}}}\cos 2\pi(Hx+Ky)\right]\ . \tag{9}$$

The observed and calculated electron-density distributions were therefore determined for the $\Sigma 5$ boundary using the 14 (H,K) reflections given in Table II, together with their nearest (h,k) lattice reflections. It was found that because the measured structure factors for this boundary were so weak and the calculated displacements were so small, the electron density from the displaced atoms could not be resolved from the electron density of the projected fcc substructure. To gain better electron-density resolution, a partial Fourier synthesis was therefore computed by omitting the lattice reflections. This is equivalent to determining the complement electron density,[34] where the complement structure (displacement field) is the difference between the superstructure (the relaxed bicrystal) and the substructure (the rigid unrelaxed bicrystal). Figures 17(a) and 17(b) show the $\Sigma 5$ complement electron-density maps projected along [001] for the observed structure factors and calculated factors, respectively. The two maps, which are seen to be very similar, show contour levels at intervals of four electrons. The primary characteristic of these maps is the presence of sharp gradients, indicated by closely spaced positive and negative contours, which are symmetrically grouped within the unit cell. These extrema in electron density are centered around atom positions that experience the largest displacements relative to the unrelaxed bicrystal. For example, sharp gradients in electron density appear at positions (0.3,0.1) and (0.4,0.2) in Figs. 17(a) and 17(b). These correspond, in the calculated structure, to a pair of atoms, one above and one below the boundary plane, that have the maximum displacements (equal to those displayed in Fig. 15). The complement syntheses therefore mirror the projected displacement field of the twist boundary, as expected. The difference synthesis of the two complement maps in Figs. 17(a) and 17(b) is illustrated in Fig. 17(c). Using the same contour scale, it is seen

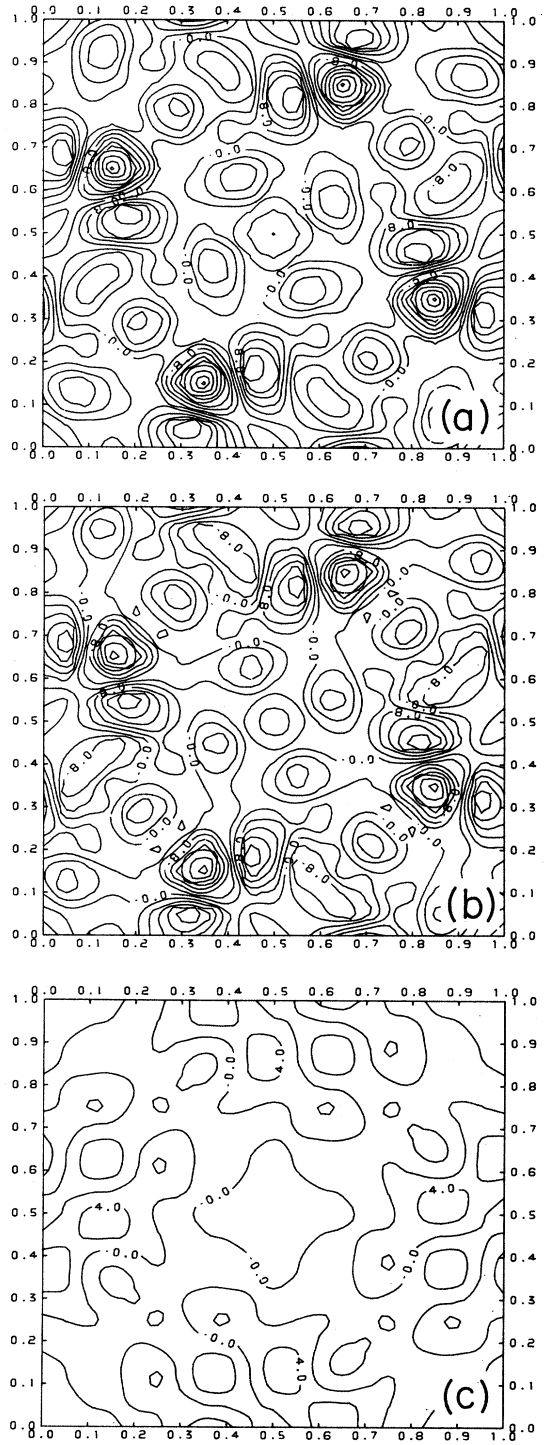

FIG. 17. Complement electron-density (difference between density of relaxed bicrystal and rigid unrelaxed bicrystal) map projected along [001] for (a) observed Σ5 static structure factors, and (b) calculated Σ5 (static embedded-atom model) structure factors. Area shown corresponds to that in Fig. 16 for Σ5. Maximum height and depth span 19 density contours. (c) Difference synthesis of the complement densities in (a) and (b). This corresponds to the difference between the densities of the observed relaxed structure and calculated relaxed structure. Maximum height and depth span only three density contours.

that there are no sharp gradients in electron density and therefore the match between the observed and calculated structures is quite good. The small (10%) undulations in electron-density difference seen in Fig. 17(c) probably reflect uncertainties in the experimental data, but may also indicate that some small refinement of the calculated structure is still necessary.

In view of the above possibility, we attempted a refinement of the calculated projected structure using the method described by Budai, Bristowe, and Sass.[9] In this procedure, the two independent atoms in the first two layers of either crystal 1 or 2 (which are not symmetry related to other atoms in these layers) are systematically moved about in a search for a structure of minimum R. The atoms were moved about on a square grid of spacing 8×10^{-4} nm over a wide range of displacements covering all physically conceivable combinations, and a "minimum-R structure" was found, having a somewhat reduced R factor, i.e., $R=0.206$. The atomic displacements for the structure are given in Table III, and the structure factors are displayed in Fig. 8(b). A comparison of Fig. 8(b) with 8(a) shows a somewhat improved agreement with the measured structure factors for the minimum-R structure, particularly for the (4,4), (2,0), and (3,3) reflections. However, of primary importance, is the result that the projected small displacements in the embedded-atom–calculated structure and the minimum-R structure are of almost exactly the same magnitudes (agreement to within 1.7×10^{-3} nm) and are in the same general directions.

In general, the results obtained in the present work (Tables I and II, and Figs. 5–13) indicate a considerable degree of consistency between the measured and calculated absolute structure factors for all five boundaries studied. The calculated results faithfully tracked the large decreases in the values of $|F_b^0|^2$, which were measured in the sequence $\Sigma113\rightarrow\Sigma25\rightarrow\Sigma13\rightarrow\Sigma17\rightarrow\Sigma5$. In addition, a considerable amount of detailed agreement between measured and calculated values of $|F_b^0|^2$ was found for the individual boundaries, particularly for the Σ113 and Σ25 boundaries, where the boundary scattering was relatively strong and could be measured more reliably. In the case of the weakly scattering Σ5 boundary, the observed structure factors led us to a most probable structure with small displacements, i.e., the minimum-R structure, which closely resembled the calculated structure. In the cases of the intermediate Σ13 and Σ17 boundaries, the very limited number of structure factors measured were reasonably consistent with corresponding calculated values. In view of this generally good consistency, we conclude that the atomistic boundary structures calculated by means of the embedded-atom model are essentially correct. These results, therefore, lend credence to this method of calculating grain-boundary structure.

Finally, we briefly compare our results with those obtained by Fitzsimmons and Sass (FS) for the Σ13 (Ref. 3) and Σ5 (Ref. 4) boundaries. For Σ13, the agreement between models is quite good. Our atomic displacement map (Fig. 14) agrees quite closely with that deduced by FS (Fig. 6 of Ref. 3) with respect to both the magnitudes and the directions of the various displacement vectors.

The extent of the agreement between the magnitudes of the maximum displacements may be seen explicitly in Fig. 15. In addition, if the relative structure factors measured by FS are normalized [on the basis of the (600) reflection] and compared with the present calculated structure factors using the embedded-atom model, an R factor equal to 0.23 is obtained.

On the other hand, our model for the $\Sigma 5$ boundary differs strongly from that of FS. In general, their displacements are much too large (see Fig. 15) and are clearly highly inconsistent with both the present experimental results and all calculated structures of this boundary using reasonable physical models. This is particularly evident in Table II and Figs. 11 and 12, where we present the calculated absolute structure factors predicted by their model. These structure factors are seen to be more than an order of magnitude too large. We therefore conclude that their model must be incorrect. This result demonstrates the difficulty of deducing a correct structure on the basis of a comparatively small number of measured relative structure factors. Further discussion of this difficulty and the strategies to deal with it may be found in Ref. 35. A more complete comparison between the predictions of the present embedded-atom model and the FS diffraction data for the $\Sigma 5$ and $\Sigma 13$ boundaries, including relrod profiles along L, is planned to be described in a forthcoming publication.

ACKNOWLEDGMENTS

We thank Dr. Mark S. Taylor and Professor B. J. Wuensch for much useful advice during the course of our work. Assistance with specimen preparation was received from Dr. T. A. Bamford. Support was provided by the U.S. Department of Energy under Grant No. DE-FG02-E7ER-43310. We are grateful to the Center for Materials Science and Engineering at the Massachusetts Institute of Technology under U.S. National Science Foundation Grant No. PNDG-84-18718-DMR for the use of its Central X-ray Facility. The embedded-atom simulation code was kindly made available to us by Dr. M. Baskes. Computer time at the Florida State University Supercomputer Computations Research Institute is gratefully acknowledged.

[1]M. Taylor, I. Majid, P. D. Bristowe, and R. W. Balluffi, this issue, the preceding paper, Phys. Rev. B **40**, 2772 (1989).
[2]M. S. Daw and M. I. Baskes, Phys. Rev. B **29**, 6443 (1984).
[3]M. R. Fitzsimmons and S. L. Sass, Acta Metall. **37**, 1009 (1989).
[4]M. R. Fitzsimmons and S. L. Sass, Acta Metall. **36**, 3103 (1988).
[5]T. Y. Tan, S. L. Sass, and R. W. Balluffi, Philos. Mag. **31**, 575 (1975).
[6]S. E. Babcock and R. W. Balluffi, Philos. Mag. A **55**, 643 (1987).
[7]S. L. Sass, J. Appl. Crystallogr. **13**, 109 (1980).
[8]P. D. Bristowe and S. L. Sass, Acta Metall. **28**, 575 (1980).
[9]J. Budai, P. D. Bristowe, and S. L. Sass, Acta Metall. **31**, 699 (1983).
[10]J. P. Hirth and J. Lothe, *Theory of Dislocations* (Wiley, New York, 1982), p. 708.
[11]W. Bollmann, *Crystal Defects and Crystalline Interfaces* (Springer-Verlag, New York, 1970), p. 148.
[12]A. Brokman and R. W. Balluffi, Acta Metall. **31**, 1639 (1983).
[13]P. D. Bristowe and A. G. Crocker, Philos Mag. A **38**, 487 (1978).
[14]Y. Oh and V. Vitek, Acta Metall. **34**, 1941 (1986).
[15]T. Schober and R. W. Balluffi, Philos Mag. **20**, 511 (1969).
[16]T. Y. Tan, J. C. M. Hwang, P. J. Goodhew, and R. W. Balluffi, Thin Solid Films **33**, 1 (1976).
[17]P. D. Bristowe and R. W. Balluffi, Surf. Sci. **144**, 14 (1984).
[18]M. C. Payne, P. D. Bristowe, and J. D. Joannopoulos, Phys. Rev. Lett. **58**, 1348 (1987).
[19]M. I. Baskes, J. Nucl. Mater. **128&129**, 676 (1984).
[20]S. M. Foiles and M. S. Daw, J. Vac. Sci. Technol. A **3**, 1565 (1985).
[21]S. M. Foiles, Phys. Rev. B **32**, 3409 (1985).
[22]M. S. Daw and R. D. Hatcher, Solid State Commun. **56**, 647 (1985).
[23]S. M. Foiles, Phys. Rev. B **32**, 7685 (1985).
[24]M. S. Daw, Surf. Sci. **166**, 2161 (1986).
[25]M. J. Stott and E. Zaremba, Phys. Rev. B **22**, 1564 (1980).
[26]M. Manninen, Phys. Rev. B **34**, 8486 (1986).
[27]K. W. Jacobson, J. K. Nørskov, and M. J. Puska, Phys. Rev. B **35**, 7423 (1987).
[28]M. W. Finnis and J. E. Sinclair, Philos Mag. A **50**, 45 (1984).
[29]S. M. Foiles, M.I. Baskes, and M. S. Daw, Phys. Rev. B **33**, 7983 (1986).
[30]I. Majid and P. D. Bristowe, Scr. Metall. **21**, 1153 (1987).
[31]M. R. Fitzsimmons, E. Burkel, and S.L. Sass, Phys. Rev. Lett. **61**, 2237 (1988).
[32]A. P. Sutton (private communication).
[33]M. J. Buerger, *Crystal-Structure Analysis* (Krieger, New York, 1980), p. 603.
[34]M.J. Buerger, *Vector Space* (Wiley, New York, 1959), p. 316.
[35]R. W. Balluffi, I. Majid, and P. D. Bristowe, in *Characterization of the Structure and Chemistry of Defects in Materials,* Mater. Res. Soc. Symp. Proc. No. 138, edited by B. C. Larson, M. Rühle, and D. N. Seidman (MRS, Pittsburgh, 1989), p. 457.

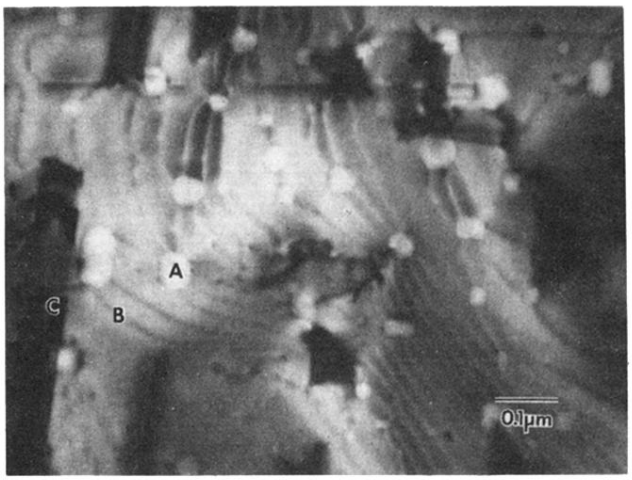

FIG. 2. Electron micrograph of typical grain-boundary area in Σ113 specimen. Visible are bubbles (at *A*), dislocations with Burgers vectors normal to the boundary (at *B*), and impinging stacking faults or thin twins (at *C*).